Direct evidence of a graded magnetic interface in bi-magnetic core/shell nanoparticles using electron magnetic circular dichroism (EMCD)

Daniel del-Pozo-Bueno[1,2,*], María Varela[3,*], Marta Estrader[4,2], Alberto López-Ortega[5,6,*], Alejandro G. Roca[7,*], Josep Nogués[7,8], Francesca Peiró[1,2], Sònia Estradé[1,2]

[1]LENS-MIND, Dept. Enginyeries Electrònica i Biomèdica, Universitat de Barcelona, Martí i Franques 1, E-08028 Barcelona, Spain.

[2]Institute of Nanoscience and Nanotechnology of the University of Barcelona (IN2UB), Av. Diagonal 645, E-08028 Barcelona, Spain.

[3]Departamento de Física de Materiales e Instituto Pluridisciplinar, Universidad Complutense de Madrid (UCM), 28040 Madrid, Spain.

[4]Departament de Química Inorgànica i Orgànica, Universitat de Barcelona, Martí i Franques 1, E-08028 Barcelona, Spain

[5]Departamento de Ciencias, Universidad Pública de Navarra, 31006 Pamplona, Spain

[6]Institute for Advanced Materials and Mathematics INAMAT, Universidad Pública de Navarra, 31006 Pamplona, Spain.

[7]Catalan Institute of Nanoscience and Nanotechnology (ICN2), CSIC and BIST, Campus UAB, Bellaterra, 08193 Barcelona, Spain.

[8]ICREA, Pg. Lluís Companys 23, E-08010 Barcelona, Spain.

[*]Corresponding authors: ddelpozo@ub.edu, mvarela@ucm.es, lopezortega.alberto@gmail.com, alejandro.gomez@icn2.cat

Abstract

Interfaces play a crucial role in composite magnetic materials and particularly in bi-magnetic core/shell nanoparticles. However, resolving the microscopic magnetic structure of these nanoparticles is rather complex. Here we investigate the local magnetization of antiferromagnetic/ferrimagnetic FeO/Fe_3O_4 core/shell nanocubes by electron magnetic circular dichroism (EMCD). The electron energy-loss spectroscopy (EELS) compositional analysis of the samples shows the presence of an oxidation gradient at the interface between the FeO core and the Fe_3O_4 shell. The EMCD measurements evidence that the nanoparticles are composed of four different zones with

distinct magnetic moment in a concentric, onion-type, structure. These magnetic areas correlate spatially with the oxidation and composition gradient, with the magnetic moment being largest at the surface and decreasing towards the core. The results show that the combination of EELS compositional mapping and EMCD can provide very valuable information of the inner magnetic structure and its correlation to the microstructure of magnetic nanoparticles.

Keywords

EMCD, EELS, Magnetic Nanoparticles, Core/Shell Nanoparticles, Graded Interfaces

Introduction

Understanding the interface structure between the different components of nano-composite structures constitutes the keystone to harness the functional properties of the material[1–8]. In particular, graded interfaces (where there is some degree of chemical intermixing between the two counterparts at the interface; also denoted as rough or interdiffused interfaces) have been shown to play a critical role in tuning the properties of diverse materials[1–7], and specifically in core/shell nanoparticles[3,9–12]. However, despite the paramount importance of interfaces, the process of gaining detailed information about them can be rather complex, since specialized tools must be used to characterize interfaces of core/shell nanoparticles at the atomic level in real space, including compositional information (e.g., transmission electron microscopy, TEM, combined with electron energy-loss spectroscopy, EELS; anomalous small angle x-ray scattering, ASAXS; extended x-ray absorption fine structure, EXAFS; or complex x-ray diffraction analysis)[11,13–15].

The degree of complexity increases in bi-magnetic core/shell nanoparticles, a widespread type of core/shell particles due to their remarkable fundamental properties and the broad range of applications. In these systems both the core and the shell exhibit magnetic properties (i.e., ferromagnetic, ferrimagnetic, antiferromagnetic)[3,7,14–16]. Here, not only the structural/morphological interface is important, but also the magnetic arrangement at the interface (e.g., strength of the exchange coupling, ferromagnetic *vs.* antiferromagnetic interface coupling, graded anisotropy or proximity effects)[12,17–19] can play a crucial role in the properties and performance of the nanoparticles. However, obtaining information of the interface magnetic structure in nanoparticles is particularly

challenging. Indirect information on the magnetic structure at the interface can sometimes be inferred from magnetization, x-ray magnetic circular dichroism (XMCD), Mössbauer spectroscopy and other techniques[20–22]. However, these techniques give information of the whole sample, thus their lack of direct spatial resolution precludes establishing a one-to-one correlation between the magnetic behavior and the structural/morphological features at the atomic scale. To obtain a straightforward correlation between the structural and magnetic interface, small angle neutron scattering (SANS) can be used, although it has been used only occasionally in bi-magnetic core/shell nanoparticles[23,24]. However, SANS averages over long lateral distances (typically, the whole sample), thus certain specifics of the structural-magnetic correlation can be easily overlooked. To gain a more microscopic insight of the structural-magnetic interface correlation, high resolution magnetic transmission electron microscopy techniques like e-holography could potentially be applied, although it has been rarely used to study bi-magnetic core/shell nanoparticles[25,26].

A very specific TEM-based technique to study the magnetic information at an atomic/nanometric length scale is energy-loss chiral magnetic dichroism, or electron magnetic circular dichroism (EMCD)[27,28]. EMCD is based on studying the difference between two EEL spectra acquired under the appropriate scattering conditions inside the TEM[27,29,30]. Although this approach allows obtaining the local magnetic moment with sub-nm precision, it has seldom been utilized on nanoparticles[29,31].

Here, we demonstrate that EMCD can disentangle the magnetic properties of iron oxide-based core/shell nanocubes, consisting of a ferrimagnetic magnetite (Fe_3O_4) shell and an antiferromagnetic wüstite (FeO) core. Combining a high spatial resolution (0.45 nm) with clustering techniques for EELS data analysis[32], the existence of a graded magnetic interface, associated to an oxidation gradient between the shell and core, is unambiguously established. It is interesting to note that an in-depth comprehension of the magnetic structure in bi-magnetic nanoparticles[3,16,18,20] and, specifically, in FeO/Fe_3O_4 core/shell systems is essential not only from a more fundamental magnetic point of view, but also for the optimization of their magnetic properties for their use in diverse fields like biomedical applications (e.g., magnetic hyperthermia or magnetic bioassays) or microwave absorbers[33–36].

Results and discussion

Morphological characterization.

The FeO/Fe_3O_4 core/shell nanoparticles, synthesized by thermal decomposition (see Methods in Supporting Information), show a rather regular square shape and a high crystallinity, with an average particle size of 29 ± 3 nm (Figure 1a). The core/shell structure was verified by means of annular bright field (ABF) and annular dark field (ADF) scanning transmission electron microscopy (STEM) images, evidencing a rather homogeneous morphology, with a shell thickness of about 5-6 nm (Figure 1b/c) along with a cubic shape core, in agreement with previous studies on similar nanoparticles[37,38]. In contrast to other oxide core/shell nanoparticles[39], it is worth noting that the core/shell structure (and oxidation states; see below) remains very stable under the current imaging conditions (200 kV acceleration voltage, beam currents of tens of pA), even after prolonged electron beam exposure. Pure Fe_3O_4 nanoparticles were also grown by thermal decomposition to serve as reference. They also show a good cubic morphology with an excellent crystallinity, and the same particle size of 29 ± 3 nm as the FeO/Fe_3O_4 core/shell nanoparticles (Figure S1).

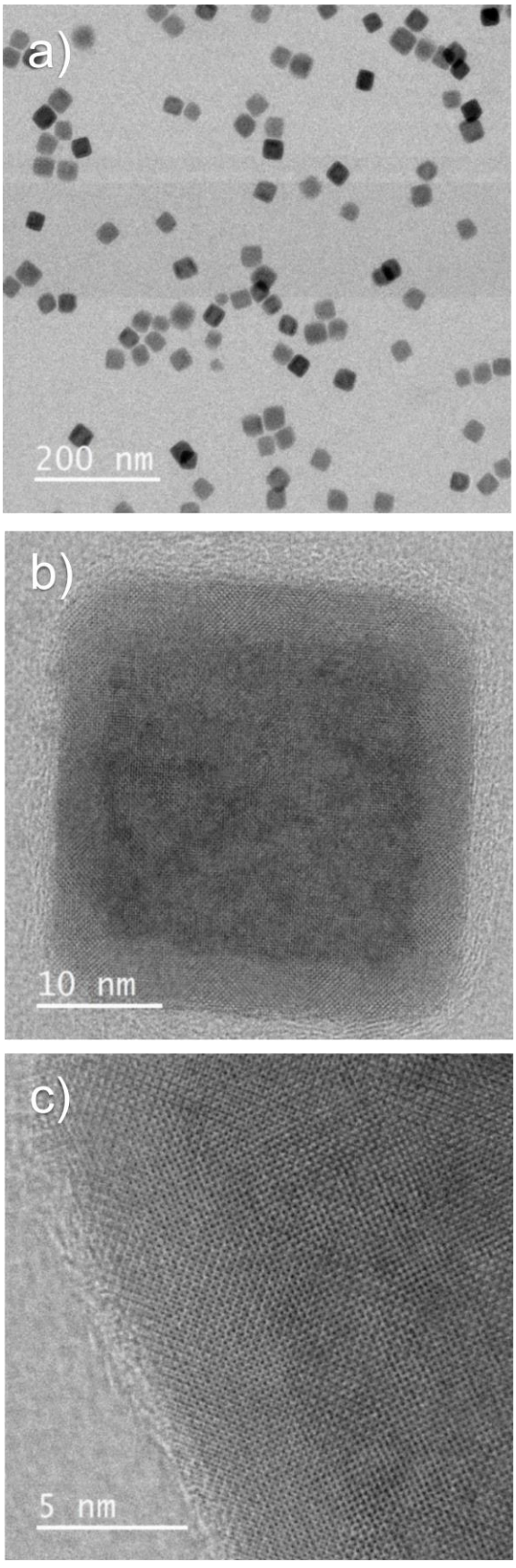

Figure 1. (a) Annular bright field (ABF) STEM image at low magnification of the FeO/Fe_3O_4 core/shell nanocubes. (b) and (c) ABF STEM images of an individual core/shell nanocube at higher magnification.

Oxidation state and compositional analysis.

Figure 2a depicts the spatial map of the Fe oxidation state obtained from the distance between the oxygen K edge and the L_3 iron white line (method ii, see Methods section in Supporting Information). Note that the signal at the left-hand side of the image corresponds to a neighboring particle. Although in the image they appear to be in contact, the particles are not overlapping as shown in Figure S2. Additional analysis of the EELS data using alternative calculation approaches[40–47] are presented in Figures S3a-c. All the four methods used show very similar results (see Methods section in Supporting Information for details). The core/shell structure can be clearly identified in these oxidation state maps. The profile of the oxidation state presented in Figure 2b (left axis), has been calculated from the mean values obtained for the four calculation methods, with an additional vertical average within the dotted box in Figure 2a, to improve signal to noise ratio. The oxidation state of the shell is close to the expected +2.65 for Fe_3O_4. On the other hand, within the core regions the value of the oxidation state is closer to +2.2, a value that is larger than the one corresponding to FeO (+2.0). This finding is probably a consequence of the measurements representing a 2D projection of 3D structure of the particles, i.e., the shell covering the core. Since the electrons must go through the whole particle (core and both upper and lower shells), the shells also contribute to the EELS signal represented in the core regions.

An elemental quantification was also extracted from the EELS data. The results are shown in the color map of Figure S3d, where it is presented the oxygen elemental composition in atomic percent (at. %). This map also evidences the core/shell structure, exhibiting an oxygen composition of about 57 at. % for the shell regions (in agreement to the magnetite stoichiometry), and an oxygen composition of around 52 at. % for the core region, which is a slightly higher than the expected stoichiometry for wüstite (50 at. %), but consistent with having the upper and lower magnetite shells. The oxygen concentration profile presented in Figure 2b (right axis) has been also calculated by averaging the corresponding values inside de dotted box in Figure 2a.

The results of these averaged quantifications (oxidation state and oxygen composition) definitely confirm the presence of an oxidation gradient near the core/shell interface extending about 3.0 ± 0.5 nm from the interface (as depicted in Figure 2b). In addition, there is an almost perfect agreement between the oxidation gradient and the composition

gradient. Thus, the sample could be better described as $FeO/Fe_xO_y/Fe_3O_4$. Note that although the presence of such a graded interface had already been proposed for FeO/Fe_3O_4 nanoparticles using diverse approaches (lattice parameter examination, x-ray analysis and Mössbauer analysis)[13,48–50]. The EELS oxidation and compositional maps give a definitive proof of the origin of the gradient, which is mainly related to the change of the oxidation state.

To further confirm the graded interface in the FeO/Fe_3O_4 nanocubes, we used principal component analysis (PCA)[51] (to reduce the noise) and k-means clustering algorithm[32] (to identify different zones in the nanoparticle) (see Methods in Supporting Information). This latter technique allows detecting areas in the nanoparticle with analogous EELS characteristics. Interestingly, the clustering algorithm identifies four concentric areas of distinct properties, i.e., inner core/outer core/inner shell/outer shell (Figure 2c). When comparing these clusters with the averaged oxidation state, the second and third clusters coincide with the oxidation and compositional gradients (Figure 2). Thus, the interface region (where the gradients are found) is identified by the clustering algorithm as two clusters, which is independently verified by the elemental quantification and oxidation state analysis. Consequently, the gradient zone is composed of two dissimilar regions, which can be interpreted as the nanoparticle being formed by a multi-shell, "onion-like", structure, $FeO/Fe_{1+x}O/Fe_{3-\delta}O_4/Fe_3O_4$, as proposed by Ichikawa *et al*.[13]

Finally, note that the pure Fe_3O_4 nanoparticles exhibit a very homogeneous oxidation state ($+2.65 \pm 0.05$; using the four analysis approaches) as well as a homogeneous oxygen composition over the whole particle (Figure S1d-e), corroborating that the graded oxidation interphase in the bi-magnetic system is an intrinsic configuration at the core-shell interface rather than to a spurious self-reduction/oxidation process of the Fe_3O_4 phase or the surrounding medium.[52,53]

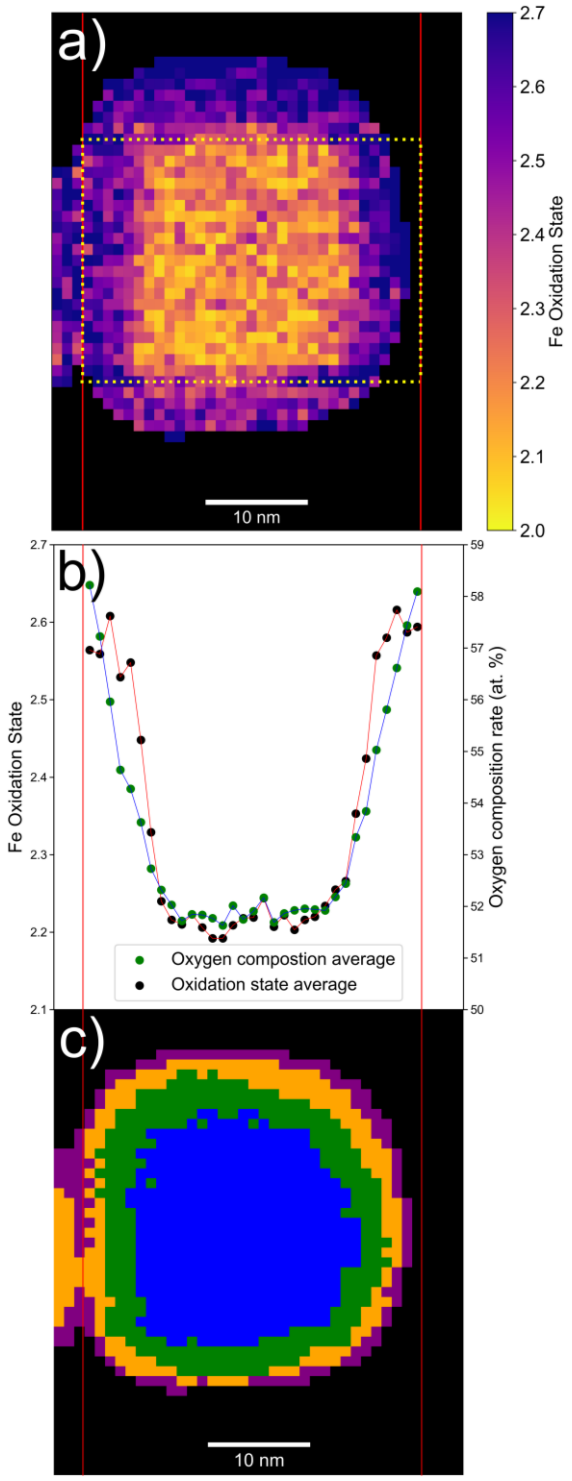

Figure 2. (a) Color map of the iron oxidation states of a FeO/Fe_3O_4 core/shell nanocube obtained from the distance between the oxygen K edge and the L_3 iron white line (method ii, see Methods section in Supporting Information). (b) Line profiles of the averaged oxidation state (black dots) and the oxygen elemental composition (green dots; see Figure S3d) (in both cases averaged vertically within the dotted box in (a), and in the first case for the four analysis methods; see Figure S3). (c) Color map with the results of the clustering analysis.

Electron magnetic circular dichroism (EMCD)

In order to investigate the effect of the graded interface on the magnetic structure of the FeO/Fe_3O_4 nanocubes we carried out an EMCD study at low temperature. Two EEL spectra with different chirality were obtained in two-beam conditions for each nanocube (see Methods in Supporting Information). The spectra correspond to the 'chiral +' (right circular polarization) and the 'chiral –' (left circular polarization), respectively. The + and – spectra were subject to the same previous corrections and clustering algorithms (see Methods in Supporting Information).

First, we analyzed several pure Fe_3O_4 nanocubes to serve as reference. The clustering analysis of the + and – spectra revealed homogenous EEL spectra over the whole sample. Figure S4 shows the EEL spectra corresponding to the two different chiralities. The spectra are clearly different (Figure S4). Subtracting the + from the – spectra we obtain the EMCD signal corresponding to the Fe_3O_4 nanocubes (Figure S4). The EMCD results obtained for the different particles are quite similar, and comparable to literature data on Fe_3O_4 films and nanoparticles[29–31].

Next, we analyzed the + and - EEL spectra for the core/shell nanocubes. Importantly, since a pixel-by-pixel comparison would be extremely complex in our case due to the weak and noisy signal and the small thermal drifts during the acquisition of the two different chiralities (resulting from small temperature fluctuations), we used the clustering algorithm to identify equivalent regions for each chirality. Note that the clustering procedure allows, in a simple and efficient way, to classify the large quantity of spectra from the nanocubes and to reduce the intrinsic noise in data by averaging all the spectra within a given cluster. As expected, the clustering results (i.e., areas with analogous characteristics) were very similar for both chiralities (Figure 3a, b). Similar to the pure Fe_3O_4 nanocubes, when comparing the EEL spectra of equivalent clusters in the two chiralities it can be clearly seen that the +/- EEL spectra are slightly different (Figures 3c-f). By subtracting the + and – spectra for the equivalent regions, we obtain the EMCD spectra of that given area (see Figure 3c-f)[54,55]. Remarkably, the EMCD spectra for all the four regions are distinctly different. This implies that the oxidation gradient induces unambiguous changes in the magnetic structure of the nanocubes. Notably, although the intensity decreases, the shape of the spectra for the four regions is somewhat similar (and similar to the Fe_3O_4 reference sample). This is somewhat expected for the surface and inner shell since they are both mainly Fe_3O_4. However, the

outer and inner regions of the core are mostly FeO, thus some changes in the EMCD spectra could potentially be anticipated. The inner FeO core should be antiferromagnetic at 100 K (Néel temperature T_N ~ 200 K; Figure S5)[37], thus no circular dichroism would be expected. Hence, the dichroic signal should arise mainly from the contribution of the Fe_3O_4 shells (since the electrons have to go through the shell before and after they probe the core). Concerning the $Fe_{1+x}O$ outer core, it is well known that the vacancies in $Fe_{1+x}O$ tend to cluster, forming Fe_3O_4-like regions inside an FeO matrix[56]. Consequently, it is not surprising that the EMCD spectrum of the $Fe_{1+x}O$ outer core is similar to the shell signals.

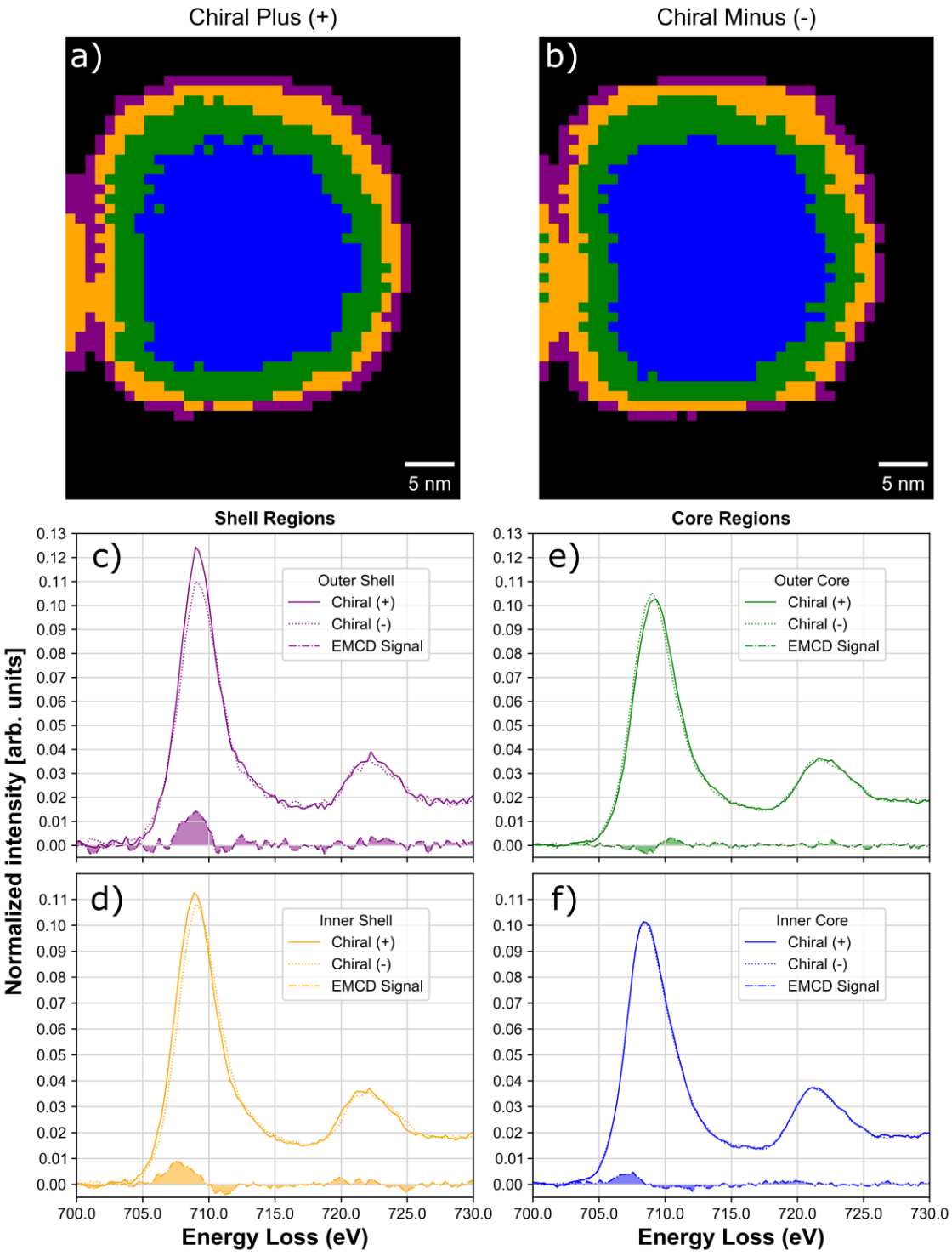

Figure 3. Color maps resulting from the clustering analysis for (a) chiral (+) and (b) chiral (-) configuration of a core/shell nanocube. (c-f) Spectra of the + and – chiralities for each section identified in the clustering and the corresponding EMCD signal: (c) outer shell (violet); (d) inner shell (orange); (e) outer core (green) and (f) inner core (blue).

To get further insight into the magnetic structure, we tried to quantify the dichroic signal of the different regions. Unfortunately, the measuring conditions do not allow to

obtain the absolute magnetic moment for each region.[57] However, since all the measurements were carried out in the same conditions, relative magnetic moments can be obtained by integrating the area of the EMCD peaks and compared among them. As can be seen in Figure 4, a clear trend emerges from the relative moments. The outer shell has the largest magnetic moment, which decreases towards the inner shell becoming smallest in the two core regions (Figure 4), evidencing that the oxidation gradient induces a magnetic gradient in the nanoparticles. However, two unusual features can be identified. First, the magnetic moment of the shell seems to be larger than the reference pure Fe_3O_4 nanocubes. This is somewhat unexpected since in pure Fe_3O_4 nanoparticles the surface tends to have lower magnetic moment than the bulk due to surface disorder.[29] Nevertheless, it is important to emphasize that magnetic moments considerably larger than bulk values have been often reported in Fe_3O_4 (and other ferrites) thin films[58–61]. These enhanced moments are typically reported to occur for very thin films or at surfaces, and are usually linked to specific defects such as grain boundaries, vacancies or antiphase boundaries[58–61]. Thus, common defects often observed in this type of (and similar) nanoparticles, such as cation inversion, lattice distortions, Fe^{+2} vacancies or grain boundaries could also contribute to the enhanced moment[37,49,62,63]. The second possible uncommon effect that can be inferred for the magnetic moment is the unusually low moment in the outer $Fe_{1+x}O$ core. Namely, due to vacancy clustering, $Fe_{1+x}O$ is expected to have larger moment than FeO. In contrast, the moment of the $Fe_{1+x}O$ region seems to be slightly smaller than the one in the FeO region. This implies that the intrinsic moment of the $Fe_{1+x}O$ outer core should be opposite to the concomitant contribution of the $Fe_{3-\delta}O_4/Fe_3O_4$ shells (arising from the path of the electrons). The simplest way to account for this effect is probably to assume an antiferromagnetic coupling between the Fe_3O_4 shell and the vacancy-induced ferrimagnetic-like spins of the core (as predicted theoretically and hinted experimentally for FeO/Fe_3O_4 and actually observed for other FeO-based systems[63–65]). In fact, this assumption could be supported by the unusually large downturn in M(T) below T_N of FeO (Figure S5). Note that antiferromagnetic core/shell interface coupling has actually been reported in other iron oxide-based bi-magnetic core/shell nanoparticles[17,66].

In addition, the overall results of the same type of analysis applied to other particles (by studying a section of the nanoparticle rather than the whole nanoparticle) were

comparable, confirming the presence of a gradual change of the oxidation state at the interface leading to a magnetic gradient (see Supporting Information; Figure S6).

Notably, this STEM-based EELS approach merging compositional and magnetic information is not only limited to oxide-based core/shell nanoparticles, but it could also be applied to other types of core/shell structures (e.g., metal/metal, metal/oxide) and to other morphologies (e.g., janus nanoparticles) or even inhomogeneous nanoparticles (e.g., phase segregation) or nanostructured composites.

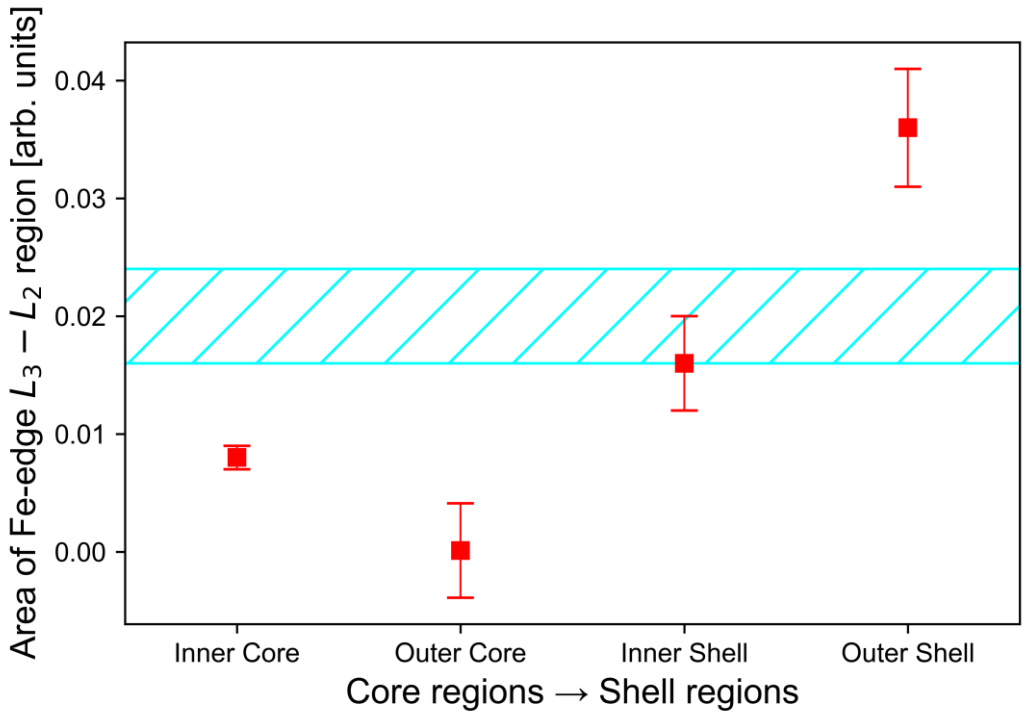

Figure 4. Area of the EMCD spectra for the different clusters. The blue region depicts the area calculated for the pure Fe_3O_4 nanocubes (see Figure S4), where the width of the band corresponds to the standard deviation of the results for the different particles.

Conclusions

In summary, we have demonstrated that the combination of EELS compositional mapping and EMCD is an excellent option to unravel the correlation between the structural/morphological and magnetic structure in bi-magnetic core/shell nanoparticles. Importantly, by using a clustering algorithm the analysis of the EMCD can be greatly simplified but still achieving nm resolution. The results show that the FeO/Fe_3O_4 nanocubes have an interdiffused interface leading to a $FeO/Fe_{1+x}O/Fe_{3-\delta}O_4/Fe_3O_4$ onion-like structure. This structure results in a graded magnetic configuration with some unusual features, like an enhanced moment for the surface Fe_3O_4 shell. These results open new avenues for studying the magnetic properties of not only complex magnetic nanoparticles but also nanostructured materials.

Acknowledgements

The authors acknowledge the financial support from the Spanish Minister of Science and Innovation (MICINN) through the projects PID2019-106165GB-C21, PID2019-106165GB-C22 and PID2019-106229RB-I00. They also acknowledge funding from Generalitat de Catalunya through the 2017-SGR-292 and 2017-SGR-776 projects. In addition, research at UCM was supported by MINECO/FEDER MAT2015-66888-C3-3-R and RTI2018-097895-B-C43 grants. And ICN2 is funded by the CERCA programme/Generalitat de Catalunya. The ICN2 is supported by the Severo Ochoa Centres of Excellence programme, funded by the Spanish Research Agency (AEI, grant no. SEV-2017-0706). M. E. thanks the Spanish MICINN and AEI/FSE for Ramón y Cajal contract (RYC2018-024396-I). A.L.O. acknowledges support from the Universidad Pública de Navarra (grant nº PJUPNA2020). STEM-EELS observations carried out at the Centro Nacional de Microscopía Electrónica at Universidad Complutense de Madrid, Spain (ICTS ELECMI).

References:

(1) Wilks, S. P. Engineering and Investigating the Control of Semiconductor Surfaces and Interfaces. *J. Phys. D: Appl. Phys.* **2002**, *35*, R77–R90. https://doi.org/https://doi.org/10.1088/0022-3727/35/9/202.

(2) Jang, Y.; Shapiro, A.; Isarov, M.; Rubin-Brusilovski, A.; Safran, A.; Budniak, A. K.; Horani, F.; Dehnel, J.; Sashchiuk, A.; Lifshitz, E. Interface Control of Electronic and Optical Properties in IV-VI and II-VI Core/Shell Colloidal Quantum Dots: A Review. *Chem. Commun.* **2017**, *53*, 1002–1024. https://doi.org/10.1039/c6cc08742f.

(3) Xu, J.; Zhu, K.; Hou, Y. Magnetic Heterostructures: Interface Control to Optimize Magnetic Property and Multifunctionality. *ACS Appl. Mater. Interfaces* **2020**, *12*, 36811–36822. https://doi.org/10.1021/acsami.0c09934.

(4) Hellman, F.; Division, M. S.; Berkeley, L.; Hoffmann, A.; Beach, G. S. D.; Fullerton, E. E.; Macdonald, A. H.; Ralph, D. C. Interface-Induced Phenomena in Magnetism. *Rev. Mod. Phys.* **2017**, *89*, 025006. https://doi.org/10.1103/RevModPhys.89.025006.

(5) Zubko, P.; Gariglio, S.; Gabay, M.; Ghosez, P.; Triscone, J. M. Interface Physics in Complex Oxide Heterostructures. *Annu. Rev. Condens. Matter Phys.* **2011**, *2*, 141–165. https://doi.org/10.1146/annurev-conmatphys-062910-140445.

(6) Huang, Z.; Ariando; Renshaw Wang, X.; Rusydi, A.; Chen, J.; Yang, H.; Venkatesan, T. Interface Engineering and Emergent Phenomena in Oxide Heterostructures. *Adv. Mater.* **2018**, *30*, 1802439. https://doi.org/10.1002/adma.201802439.

(7) Laureti, S.; Gerardino, A.; Dacapito, F.; Peddis, D.; Varvaro, G. The Role of Chemical and Microstructural Inhomogeneities on Interface Magnetism. *Nanotechnology* **2021**, *32*, 205701. https://doi.org/10.1088/1361-6528/abe260.

(8) Fallarino, L.; Kirby, B.; Fullerton, E. Graded Magnetic Materials. *J. Phys. D: Appl. Phys.* **2021**, *54*, 303002. https://doi.org/10.1088/1361-6463/abfad3.

(9) Chen, Y.; Jiang, H.; Li, L.; Wang, Q.; Du, L.; Liu, X.; Tian, G. Hierarchical NiS Decorated CuO@$ZnFe_2O_4$ Nanoarrays as Advanced Photocathodes for Hydrogen Evolution Reaction. *Int. J. Hydrogen Energy* **2020**, *45*, 6174–6183. https://doi.org/10.1016/j.ijhydene.2019.12.170.

(10) Hu, L.; Brüner, P.; Grehl, T.; Brongersma, H. H.; Cabana, J. Control of Chemical Structure in Core-Shell Nanocrystals for the Stabilization of Battery Electrode/Electrolyte Interfaces. *Chem. Mater.* **2017**, *29*, 5896–5905. https://doi.org/10.1021/acs.chemmater.7b01269.

(11) Boldt, K.; Bartlett, S.; Kirkwood, N.; Johannessen, B. Quantification of Material Gradients in Core/Shell Nanocrystals Using EXAFS Spectroscopy. *Nano Lett.* **2020**, *20*, 1009–1017. https://doi.org/10.1021/acs.nanolett.9b04143.

(12) López-Ortega, A.; Estrader, M.; Salazar-Alvarez, G.; Estradé, S.; Golosovsky, I. V.; Dumas, R. K.; Keavney, D. J.; Vasilakaki, M.; Trohidou, K. N.; Sort, J.; Peiró, F.;

Suriñach, S.; Baró, M. D.; Nogués, J. Strongly Exchange Coupled Inverse Ferrimagnetic Soft/Hard, $Mn_xFe_{3-x}O_4/Fe_xMn_{3-x}O_4$, Core/Shell Heterostructured Nanoparticles. *Nanoscale* **2012**, *4*, 5138–5147. https://doi.org/10.1039/c2nr30986f.

(13) Ichikawa, R. U.; Roca, A. G.; López-Ortega, A.; Estrader, M.; Peral, I.; Turrillas, X.; Nogués, J. Combining X-Ray Whole Powder Pattern Modeling, Rietveld and Pair Distribution Function Analyses as a Novel Bulk Approach to Study Interfaces in Heteronanostructures: Oxidation Front in FeO/Fe_3O_4 Core/Shell Nanoparticles as a Case Study. *Small* **2018**, *14*, 1800804. https://doi.org/10.1002/smll.201800804.

(14) Muro-Cruces, J.; Roca, A. G.; López-Ortega, A.; Fantechi, E.; Del-Pozo-Bueno, D.; Estradé, S.; Peiró, F.; Sepúlveda, B.; Pineider, F.; Sangregorio, C.; Nogues, J. Precise Size Control of the Growth of Fe_3O_4 Nanocubes over a Wide Size Range Using a Rationally Designed One-Pot Synthesis. *ACS Nano* **2019**, *13*, 7716-7728. https://doi.org/10.1021/acsnano.9b01281.

(15) Krycka, K. L.; Borchers, J. A.; Salazar-Alvarez, G.; López-Ortega, A.; Estrader, M.; Estradé, S.; Winkler, E.; Zysler, R. D.; Sort, J.; Peiró, F.; Baró, M. D.; Kao, C. C.; Nogués, J. Resolving Material-Specific Structures within $Fe_3O_4|\gamma\text{-}Mn_2O_3$ Core|shell Nanoparticles Using Anomalous Small-Angle X-Ray Scattering. *ACS Nano* **2013**, *7*, 921–931. https://doi.org/10.1021/nn303600e.

(16) Winkler, E. L.; Zysler, R. D. Core/Shell Bimagnetic Nanoparticles. In *New Trends in Nanoparticle Magnetism*; Springer International Publishing: Cham, Switzerland, **2021**, pp. 87-106. https://doi.org/10.1007/978-3-030-60473-8_4.

(17) Estrader, M.; López-Ortega, A.; Estradé, S.; Golosovsky, I. V.; Salazar-Alvarez, G.; Vasilakaki, M.; Trohidou, K. N.; Varela, M.; Stanley, D. C.; Sinko, M.; Pechan, M. J.; Keavney, D. J.; Peiró, F.; Suriñach, S.; Baró, M. D.; Nogués, J. Robust Antiferromagnetic Coupling in Hard-Soft Bi-Magnetic Core/Shell Nanoparticles. *Nat. Commun.* **2013**, *4*, 2960. https://doi.org/10.1038/ncomms3960.

(18) Lavorato, G. C.; Das, R.; Masa, A. Hybrid Magnetic Nanoparticles as Efficient Nanoheaters in Biomedical Applications. *Nanoscale Adv.* **2021**, *3*, 867-888. https://doi.org/10.1039/d0na00828a.

(19) De Toro, J. A.; Marques, D. P.; Muñiz, P.; Skumryev, V.; Sort, J.; Givord, D.; Nogués, J. High Temperature Magnetic Stabilization of Cobalt Nanoparticles by an Antiferromagnetic Proximity Effect. *Phys. Rev. Lett.* **2015**, *115*, 57201. https://doi.org/10.1103/PhysRevLett.115.057201.

(20) López-Ortega, A.; Estrader, M.; Salazar-Alvarez, G.; Roca, A. G.; Nogués, J. Applications of Exchange Coupled Bi-Magnetic Hard/Soft and Soft/Hard Magnetic Core/Shell Nanoparticles. *Phys. Rep.* **2015**, *553*, 1–32. https://doi.org/10.1016/j.physrep.2014.09.007.

(21) Kamzin, A. S.; Obaidat, I. M.; Valliulin, A. A.; Semenov, V. G.; Al-Omari, I. A. The Composition and Magnetic Structure of $Fe_3O_4/\gamma\text{-}Fe_2O_3$ Core–Shell Nanocomposites at 300 and 80 K: Mössbauer Study (Part I). *Phys. Solid State* **2020**, *62*, 1933–1943. https://doi.org/10.1134/S1063783420100157.

(22) Juhin, A.; López-Ortega, A.; Sikora, M.; Carvallo, C.; Estrader, M.; Estradé, S.; Peiró, F.; Baró, M. D.; Sainctavit, P.; Glatzel, P.; Nogués, J. Direct Evidence for an Interdiffused Intermediate Layer in Bi-magnetic Core-Shell Nanoparticles. *Nanoscale* **2014**, *6*, 11911–11920. https://doi.org/10.1039/c4nr02886d.

(23) Oberdick, S. D.; Abdelgawad, A.; Moya, C.; Mesbahi-Vasey, S.; Kepaptsoglou, D.; Lazarov, V. K.; Evans, R. F. L.; Meilak, D.; Skoropata, E.; Van Lierop, J.; Hunt-Isaak, I.; Pan, H.; Ijiri, Y.; Krycka, K. L.; Borchers, J. A.; Majetich, S. A. Spin Canting across Core/Shell $Fe_3O_4/Mn_xFe_{3-x}O_4$ Nanoparticles. *Sci. Rep.* **2018**, *8*, 3425. https://doi.org/10.1038/s41598-018-21626-0.

(24) Krycka, K. L.; Borchers, J. A.; Laver, M.; Salazar-Alvarez, G.; López-Ortega, A.; Estrader, M.; Suriñach, S.; Baró, M. D.; Sort, J.; Nogoués, J. Correlating Material-Specific Layers and Magnetic Distributions within Onion-like $Fe_3O_4/MnO/\gamma\text{-}Mn_2O_3$ Core/Shell Nanoparticles. *J. Appl. Phys.* **2013**, *113*, 17B531. https://doi.org/10.1063/1.4801423.

(25) Pichon, B. P.; Gerber, O.; Lefevre, C.; Florea, I.; Fleutot, S.; Baaziz, W.; Pauly, M.; Ohlmann, M.; Ulhaq, C.; Ersen, O.; Pierron-Bohnes, V.; Panissod, P.; Drillon, M.; Begin-Colin, S. Microstructural and Magnetic Investigations of Wüstite-Spinel Core-Shell Cubic-Shaped Nanoparticles. *Chem. Mater.* **2011**, *23*, 2886–2900. https://doi.org/10.1021/cm2003319.

(26) Yang, M. Da; Ho, C. H.; Ruta, S.; Chantrell, R.; Krycka, K.; Hovorka, O.; Chen, F. R.; Lai, P. S.; Lai, C. H. Magnetic Interaction of Multifunctional Core–Shell Nanoparticles for Highly Effective Theranostics. *Adv. Mater.* **2018**, *30*, 1802444. https://doi.org/10.1002/adma.201802444.

(27) Rubino, S.; Schattschneider, P.; Stöger-Pollach, M.; Hébert, C.; Rusz, J.; Calmels, L.; Warot-Fonrose, B.; Houdellier, F.; Serin, V.; Novak, P. Energy-Loss Magnetic Chiral Dichroism (EMCD): Magnetic Chiral Dichroism in the Electron Microscope. *J. Mater. Res.* **2008**, *23*, 2582–2590. https://doi.org/10.1557/jmr.2008.0348.

(28) Schattschneider, P.; Stöger-pollach, M.; Rubino, S.; Sperl, M.; Hurm, C.; Zweck, J.; Rusz, J. Detection of Magnetic Circular Dichroism on the Two-Nanometer Scale. *Phys. Rev. B: Condens. Matter Mater. Phys.* **2008**, *78*, 104413. https://doi.org/10.1103/PhysRevB.78.104413.

(29) Salafranca, J.; Gazquez, J.; Pérez, N.; Labarta, A.; Pantelides, S. T.; Pennycook, S. J.; Batlle, X.; Varela, M. Surfactant Organic Molecules Restore Magnetism in Metal-Oxide Nanoparticle Surfaces. *Nano Lett.* **2012**, *12*, 2499–2503. https://doi.org/10.1021/nl300665z.

(30) Thersleff, T.; Rusz, J.; Rubino, S.; Hjörvarsson, B.; Ito, Y.; Zaluzec, N.; Leifer, K. Quantitative Analysis of Magnetic Spin and Orbital Moments from an Oxidized Iron (1 1 0) Surface Using Electron Magnetic Circular Dichroism. *Sci. Rep.* **2015**, *5*, 13012. https://doi.org/10.1038/srep13012.

(31) Stöger-Pollach, M.; Treiber, C. D.; Resch, G. P.; Keays, D. A.; Ennen, I. EMCD Real Space Maps of Magnetospirillum Magnetotacticum. *Micron* **2011**, *42*, 456–460. https://doi.org/10.1016/j.micron.2011.01.003.

(32) Torruella, P.; Estrader, M.; López-Ortega, A.; Baró, M. D.; Varela, M.; Peiró, F.; Estradé, S. Clustering Analysis Strategies for Electron Energy Loss Spectroscopy (EELS). *Ultramicroscopy* **2018**, *185*, 42–48. https://doi.org/10.1016/j.ultramic.2017.11.010.

(33) Lak, A.; Cassani, M.; Mai, B. T.; Winckelmans, N.; Cabrera, D.; Sadrollahi, E.; Marras, S.; Remmer, H.; Fiorito, S.; Cremades-Jimeno, L.; Litterst, F. J.; Ludwig, F.; Manna, L.; Teran, F. J.; Bals, S.; Pellegrino, T. Fe^{2+} Deficiencies, FeO Subdomains, and Structural Defects Favor Magnetic Hyperthermia Performance of Iron Oxide Nanocubes into Intracellular Environment. *Nano Lett.* **2018**, *18*, 6856–6866. https://doi.org/10.1021/acs.nanolett.8b02722.

(34) Khurshid, H.; Alonso, J.; Nemati, Z.; Phan, M. H.; Mukherjee, P.; Fdez-Gubieda, M. L.; Barandiarán, J. M.; Srikanth, H. Anisotropy Effects in Magnetic Hyperthermia: A Comparison between Spherical and Cubic Exchange-Coupled FeO/Fe_3O_4 Nanoparticles. *J. Appl. Phys.* **2015**, *117*, 17A337. https://doi.org/10.1063/1.4919250.

(35) Zheng, J.; Yu, Z.; Ji, G.; Lin, X.; Lv, H.; Du, Y. Reduction Synthesis of $Fe_xO_y@SiO_2$ Core-Shell Nanostructure with Enhanced Microwave-Absorption Properties. *J. Alloys Compd.* **2014**, *602*, 8–15. https://doi.org/10.1016/j.jallcom.2014.03.002.

(36) Lak, A.; Dieckhoff, J.; Ludwig, F.; Scholtyssek, J. M.; Goldmann, O.; Lünsdorf, H.; Eberbeck, D.; Kornowski, A.; Kraken, M.; Litterst, F. J.; Fiege, K.; Mischnick, P.; Schilling, M. Highly Stable Monodisperse PEGylated Iron Oxide Nanoparticle Aqueous Suspensions: A Nontoxic Tracer for Homogeneous Magnetic Bioassays. *Nanoscale* **2013**, *5*, 11447–11455. https://doi.org/10.1039/c3nr02197a.

(37) Estrader, M.; López-Ortega, A.; Golosovsky, I. V.; Estradé, S.; Roca, A. G.; Salazar-Alvarez, G.; López-Conesa, L.; Tobia, D.; Winkler, E.; Ardisson, J. D.; Macedo, W. A. A.; Morphis, A.; Vasilakaki, M.; Trohidou, K. N.; Gukasov, A.; Mirebeau, I.; Makarova, O. L.; Zysler, R. D.; Peiró, F.; Baró, M. D.; Bergström, L.; Nogués, J. Origin of the Large Dispersion of Magnetic Properties in Nanostructured Oxides: Fe_xO/Fe_3O_4 Nanoparticles as a Case Study. *Nanoscale* **2015**, *7*, 3002–3015. https://doi.org/10.1039/C4NR06351A.

(38) Torruella, P.; Arenal, R.; De La Peña, F.; Saghi, Z.; Yedra, L.; Eljarrat, A.; López-Conesa, L.; Estrader, M.; López-Ortega, A.; Salazar-Alvarez, G.; Nogués, J.; Ducati, C.; Midgley, P. A.; Peiró, F.; Estradé, S. 3D Visualization of the Iron Oxidation State in FeO/Fe_3O_4 Core-Shell Nanocubes from Electron Energy Loss Tomography. *Nano Lett.* **2016**, *16*, 5068–5073. https://doi.org/10.1021/acs.nanolett.6b01922.

(39) Roldan, M. A.; Mayence, A.; López-Ortega, A.; Ishikawa, R.; Salafranca, J.; Estrader, M.; Salazar-Alvarez, G.; Dolors Baró, M.; Nogués, J.; Pennycook, S. J.; Varela, M. Probing the Meta-Stability of Oxide Core/Shell Nanoparticle Systems at Atomic Resolution. *Chem. Eng. J.* **2021**, *405*, 126820. https://doi.org/10.1016/j.cej.2020.126820.

(40) Colliex, C.; Manoubi, T.; Ortiz, C. Electron-Energy-Loss-Spectroscopy near-Edge Fine Structures in the Iron-Oxygen System. *Phys. Rev. B: Condens. Matter Mater. Phys.* **1991**, *44*, 11402–11411. https://doi.org/10.1103/PhysRevB.44.11402.

(41) Varela, M.; Oxley, M. P.; Luo, W.; Tao, J.; Watanabe, M.; Lupini, A. R.; Pantelides, S. T.; Pennycook, S. J. Atomic-Resolution Imaging of Oxidation States in Manganites. *Phys. Rev. B: Condens. Matter Mater. Phys.* **2009**, *79*, 085117. https://doi.org/10.1103/PhysRevB.79.085117.

(42) Tan, H.; Verbeeck, J.; Abakumov, A.; van Tendeloo, G. Oxidation State and Chemical Shift Investigation in Transition Metal Oxides by EELS. *Ultramicroscopy* **2012**, *116*, 24–33. https://doi.org/10.1016/j.ultramic.2012.03.002.

(43) Yedra, L.; Xuriguera, E.; Estrader, M.; López-Ortega, A.; Baró, M. D.; Nogués, J.; Roldan, M.; Varela, M.; Estradé, S.; Peiró, F. Oxide Wizard: An EELS Application to Characterize the White Lines of Transition Metal Edges. *Microsc. Microanal.* **2014**, *20*, 698–705. https://doi.org/10.1017/S1431927614000440.

(44) Arévalo-López, Á. M.; Alario-Franco, M. Á. Reliable Method for Determining the Oxidation State in Chromium Oxides. *Inorg. Chem.* **2009**, *48*, 11843–11846. https://doi.org/10.1021/ic901887y.

(45) Luo, K.; Roberts, M. R.; Hao, R.; Guerrini, N.; Pickup, D. M.; Liu, Y. S.; Edström, K.; Guo, J.; Chadwick, A. v.; Duda, L. C.; Bruce, P. G. Charge-Compensation in 3d-Transition-Metal-Oxide Intercalation Cathodes through the Generation of Localized Electron Holes on Oxygen. *Nat. Chem.* **2016**, *8*, 684–691. https://doi.org/10.1038/nchem.2471.

(46) van Aken, P. A.; Liebscher, B. Quantification of Ferrous/Ferric Ratios in Minerals: New Evaluation Schemes of Fe L_{23} Electron Energy-Loss near-Edge Spectra. *Phys. Chem. Miner.* **2002**, *29*, 188–200. https://doi.org/10.1007/s00269-001-0222-6.

(47) Calvert, C. C.; Brown, A.; Brydson, R. Determination of the Local Chemistry of Iron in Inorganic and Organic Materials. *J. Electron Spectrosc. Relat. Phenom.* **2005**, *143*, 173–187. https://doi.org/10.1016/j.elspec.2004.03.012.

(48) Pichon, B. P.; Gerber, O.; Lefevre, C.; Florea, I.; Fleutot, S.; Baaziz, W.; Pauly, M.; Ohlmann, M.; Ulhaq, C.; Ersen, O.; Pierron-Bohnes, V.; Panissod, P.; Drillon, M.; Begin-Colin, S. Microstructural and Magnetic Investigations of Wüstite-Spinel Core-Shell Cubic-Shaped Nanoparticles. *Chem. Mater.* **2011**, *23*, 2886–2900. https://doi.org/10.1021/cm2003319.

(49) Wetterskog, E.; Tai, C. W.; Grins, J.; Bergström, L.; Salazar-Alvarez, G. Anomalous Magnetic Properties of Nanoparticles Arising from Defect Structures: Topotaxial Oxidation of $Fe_{1-x}O|Fe_{3-\delta}O_4$ Core|shell Nanocubes to Single-Phase Particles. *ACS Nano* **2013**, *7*, 7132–7144. https://doi.org/10.1021/nn402487q.

(50) Castellanos-Rubio, I.; Rodrigo, I.; Munshi, R.; Arriortua, O.; Garitaonandia, J. S.; Martinez-Amesti, A.; Plazaola, F.; Orue, I.; Pralle, A.; Insausti, M. Outstanding Heat Loss via Nano-Octahedra above 20 Nm in Size: From Wustite-Rich Nanoparticles to Magnetite Single-Crystals. *Nanoscale* **2019**, *11*, 16635–16649. https://doi.org/10.1039/c9nr04970c.

(51) Cueva, P.; Hovden, R.; Mundy, J. A.; Xin, H. L.; Muller, D. A. Data Processing for Atomic Resolution Electron Energy Loss Spectroscopy. *Microsc. Microanal.* **2012**, *18*, 667–675. https://doi.org/10.1017/S1431927612000244.

(52) López-Ortega, A.; Roca, A. G.; Torruella, P.; Petrecca, M.; Estradé, S.; Peiró, F.; Puntes, V.; Nogués, J. Galvanic Replacement onto Complex Metal-Oxide Nanoparticles: Impact of Water or Other Oxidizers in the Formation of Either Fully Dense Onion-like or Multicomponent Hollow MnO_x/FeO_x Structures. *Chem. Mater.* **2016**, *28*, 8025–8031. https://doi.org/10.1021/acs.chemmater.6b03765.

(53) García-García, S.; López-Ortega, A.; Zheng, Y.; Nie, Y.; Cho, K.; Chuvilin, A.; Knez, M. Ligand-Induced Reduction Concerted with Coating by Atomic Layer Deposition on the Example of TiO_2-Coated Magnetite Nanoparticles. *Chem. Sci.* **2019**, *10*, 2171–2178. https://doi.org/10.1039/c8sc04474k.

(54) Wang, Z. Q.; Zhong, X. Y.; Yu, R.; Cheng, Z. Y.; Zhu, J. Quantitative Experimental Determination of Site-Specific Magnetic Structures by Transmitted Electrons. *Nat. Commun.* **2013**, *4*, 1395. https://doi.org/10.1038/ncomms2323.

(55) Peña, F. de la; Prestat, E.; Fauske, V. T.; Burdet, P.; Furnival, T.; Jokubauskas, P.; Lähnemann, J.; Nord, M.; Ostasevicius, T.; MacArthur, K. E.; Johnstone, D. N.; Sarahan, M.; Taillon, J.; Aarholt, T.; Migunov, V.; Eljarrat, A.; Caron, J.; Poon, T.; Mazzucco, S.; Martineau, B.; Somnath, S.; Slater, T.; Francis, C.; Tappy, N.; Walls, M.; Cautaerts, N.; Winkler, F.; Donval, G. Hyperspy/Hyperspy: Release v1.6.4. **2021**. https://doi.org/10.5281/ZENODO.5082777.

(56) Gavarri, J. R.; Carel, C. The Complex Nonstoichiometry of Wüstite $Fe_{1-z}O$: Review and Comments. *Prog. Solid State Chem.* **2019**, *53*, 27–49. https://doi.org/10.1016/j.progsolidstchem.2018.10.001.

(57) Rusz, J.; Oppeneer, P. M.; Lidbaum, H.; Rubino, S.; Leifer, K. Asymmetry of the Two-Beam Geometry in EMCD Experiments. *J. Microsc.* **2010**, *237*, 465–468. https://doi.org/10.1111/j.1365-2818.2009.03295.x.

(58) Pohlmann, T.; Kuschel, T.; Rodewald, J.; Thien, J.; Ruwisch, K.; Bertram, F.; Weschke, E.; Shafer, P.; Wollschläger, J.; Küpper, K. Cation- And Lattice-Site-Selective Magnetic Depth Profiles of Ultrathin Fe_3O_4 (0 0 1) Films. *Phys. Rev. B: Condens. Matter Mater. Phys.* **2020**, *102*, 220411. https://doi.org/10.1103/PhysRevB.102.220411.

(59) Phase, D. M.; Panchal, G.; Rawat, R.; Tiwari, S.; Prakash, R.; Jain, D.; Choudhary, R. J. Anomalous Magnetic Properties of Fe_3O_4 Nanostructures on GaAs Substrate Probed Using X-Ray Magnetic Circular Dichroism. *J. Magn. Magn. Mater.* **2019**, *482*, 296–300. https://doi.org/10.1016/j.jmmm.2019.03.041.

(60) Guan, X.; Zhou, G.; Xue, W.; Quan, Z.; Xu, X. The Investigation of Giant Magnetic Moment in Ultrathin Fe_3O_4 Films. *APL Mater.* **2016**, *4*, 36104. https://doi.org/10.1063/1.4944590.

(61) Herng, T. S.; Xiao, W.; Poh, S. M.; He, F.; Sutarto, R.; Zhu, X.; Li, R.; Yin, X.; Diao, C.; Yang, Y.; Huang, X.; Yu, X.; Feng, Y. P.; Rusydi, A.; Ding, J. Achieving a High Magnetization in Sub-Nanostructured Magnetite Films by Spin-Flipping of Tetrahedral

Fe^{3+} Cations. *Nano Res.* **2015**, *8*, 2935–2945. https://doi.org/10.1007/s12274-015-0798-7.

(62) Torruella, P.; Ruiz-Caridad, A.; Walls, M.; Roca, A. G.; López-Ortega, A.; Blanco-Portals, J.; López-Conesa, L.; Nogués, J.; Peiró, F.; Estradé, S. Atomic-Scale Determination of Cation Inversion in Spinel-Based Oxide Nanoparticles. *Nano Lett.* **2018**, *18*, 5854–5861. https://doi.org/10.1021/acs.nanolett.8b02524.

(63) Lappas, A.; Antonaropoulos, G.; Brintakis, K.; Vasilakaki, M.; Trohidou, K. N.; Iannotti, V.; Ausanio, G.; Kostopoulou, A.; Abeykoon, M.; Robinson, I. K.; Bozin, E. S. Vacancy-Driven Noncubic Local Structure and Magnetic Anisotropy Tailoring in Fe_xO-$Fe_{3-\delta}O_4$ Nanocrystals. *Phys. Rev. X* **2019**, *9*, 041044. https://doi.org/10.1103/PhysRevX.9.041044.

(64) Novotny, Z.; Mulakaluri, N.; Edes, Z.; Schmid, M.; Pentcheva, R.; Diebold, U.; Parkinson, G. S. Probing the Surface Phase Diagram of Fe_3O_4 (0 0 1) towards the Fe-Rich Limit: Evidence for Progressive Reduction of the Surface. *Phys. Rev. B: Condens. Matter Mater. Phys.* **2013**, *87*, *195410*. https://doi.org/10.1103/PhysRevB.87.195410.

(65) Wang, B. Y.; Chen, C. J.; Lin, K.; Hsu, C. Y.; Ning, J. Y.; Tsai, M. S.; Chuang, T. H.; Wei, D. H.; Weng, S. C. Promoting Exchange Bias Coupling in Fe/MgO (0 0 1) Films by Controlling Interface Oxide Distribution. *Appl. Surf. Sci.* **2020**, *533*, 147501. https://doi.org/10.1016/j.apsusc.2020.147501.

(66) Kons, C.; Phan, M. H.; Srikanth, H.; Arena, D. A.; Nemati, Z.; Borchers, J. A.; Krycka, K. L. Investigating Spin Coupling across a Three-Dimensional Interface in Core/Shell Magnetic Nanoparticles. *Phys. Rev. Mater.* **2020**, *4*, 034408. https://doi.org/10.1103/PhysRevMaterials.4.034408.

Supplementary information

This material is available free of charge via the internet at http://pubs.acs.org. The supplementary information contains descriptions and details of the experimental methods: the nanoparticles shynthesis, the morphological characterization, the electron energy-loss spectroscopy, the determination of oxidation state, the determination of the elemental compostion, the electron magnetic circular dichroism technique, and the magnetic characterization. It also includes the additional figures from S1 to S9.

Table of Content (ToC)